Satellite Altimetry Over Oceans and Land Surfaces
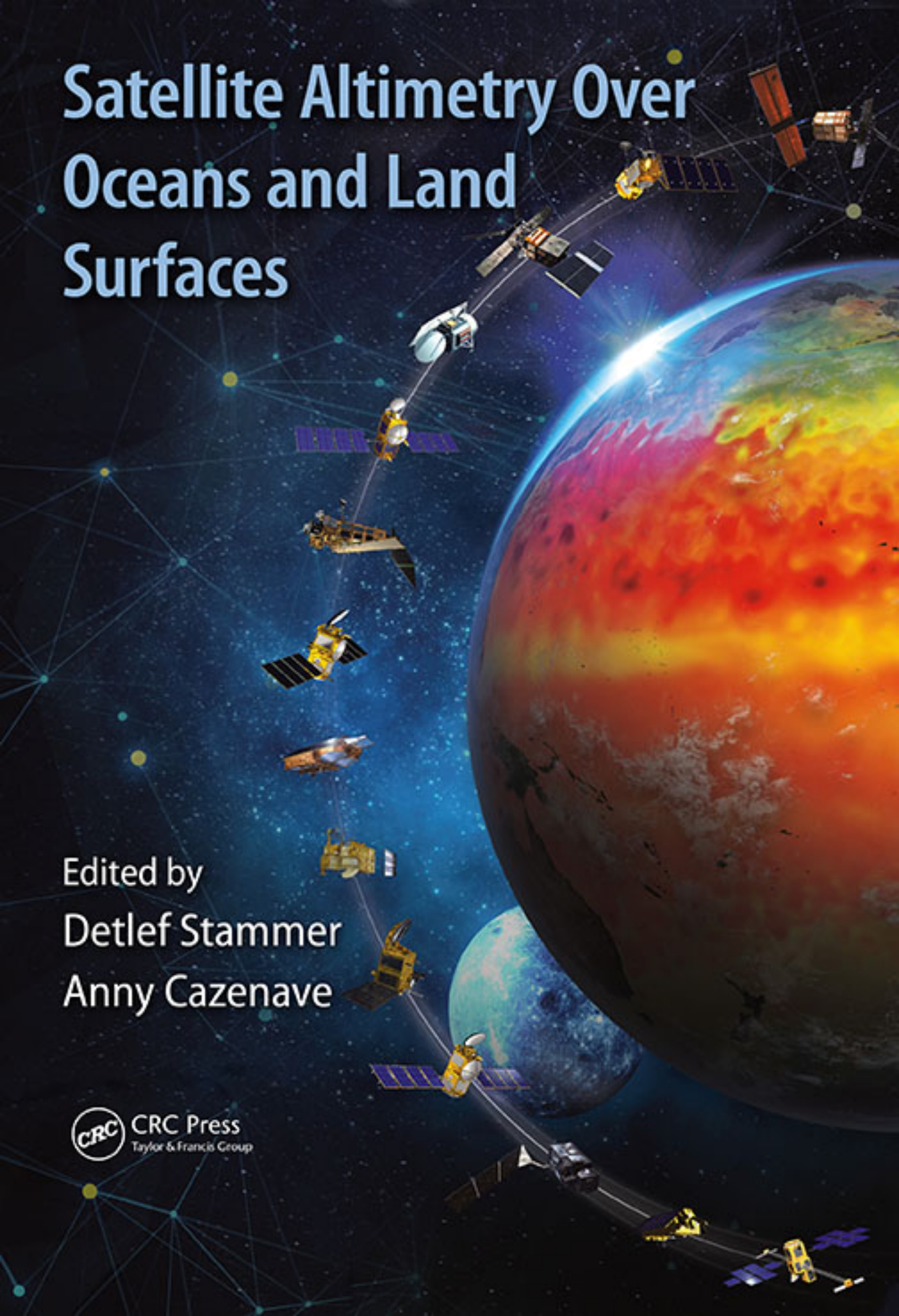
Edited by
Detlef Stammer
Anny Cazenave

16 Advances in Imaging Small-Scale Seafloor and Sub-Seafloor Tectonic Fabric Using Satellite Altimetry

R. Dietmar Mueller, Kara J. Matthews, and David T. Sandwell

CONTENTS

Key words: tectonics, microplates, fracture zone, passive margin, sedimentary basin, fault, mid-ocean ridge

16.1 INTRODUCTION

In this chapter, we first review advances in satellite altimetry for imaging small-scale structures on the seafloor, focusing on oceanic microplates and fracture zones, followed by imaging fault systems on stretched continental crust. The two examples we focus on are on the Falkland Plateau and the Lord Howe Rise, both stretched, submerged continental plateaus where satellite altimetry data now allow the mapping of detailed fault fabrics. We also review the utility of satellite altimetry data for understanding the timing and nature of major tectonic reorganizations in the ocean basins.

16.2   SATELLITE-DERIVED GRAVITY FOR TECTONIC MAPPING

16.2.1   Brief History

There are two approaches for mapping the topography and thus the tectonics of the deep ocean. Shipboard surveys, using multibeam sonar technology, provide the highest resolution (approximately 100 m) and accuracy (approximately 10 m) but to date only about 11% of the deep ocean has been mapped with this technology. Another 5.5% of the seafloor has been mapped by older, single-beam sonars that offer only about 1000 m spatial resolution. These older data are critical for filling large coverage gaps in the most remote ocean areas. The topography of the remaining 83% of the seafloor is mapped at low resolution (approximately 6000 m) from satellite-derived gravity. This is possible because the topography of the seafloor represents a large contrast in density between the seawater and the rock. Topographic highs associated with, for example, ridges or seamounts have an extra mass relative to the surrounding seafloor. This extra mass produces a local increase in the pull of gravity or a gravity anomaly. Moreover, seafloor topography that is buried by lower density sediments will also produce gravity anomalies because the sediments have a lower density than the basement rock. Thus, an accurate mapping of the gravity field can be used to infer seafloor topography even if it is buried by sediment.

Satellite altimeters can provide high spatial resolution maps of the ocean surface topography, which to a first approximation is an equipotential surface called the geoid. As will be discussed, the geoid maps can be converted to maps of gravity anomaly and thus can reveal the tectonics of the seafloor. The accuracy and resolution of these altimeter-derived maps depend on three factors: spatial track density, altimeter range precision, and diverse track orientation. Over the past 40 years, there have been a number of altimeter missions having the ability to map seafloor tectonics but only a few missions have the dense track coverage needed for mapping at high spatial resolution. Next, we review the significant milestones in tectonic mapping from altimetry.

Seasat: The first such maps were provided by the Seasat altimeter mission (NASA 1978). Although the satellite failed after just 90 days in orbit, the gravity maps constructed by Haxby et al. (1983) revolutionized our understanding of deep ocean tectonics. In particular, the Seasat gravity maps revealed large, previously unknown seamount chains in the southern oceans as well as a more accurate mapping of the plate boundaries.

ERS-1 and GEOSAT: In mid-1995, better altimeter coverage became available from the European Remote Sensing (ERS) 1 altimeter (European Space Agency) and the GEOSAT altimeter (U.S. Navy). The GEOSAT satellite, launched in 1985, collected high-precision sea surface height measurements in a non-repeat orbit for 1.5 years and continued in a repeating orbit for another three years. These data remained classified until the ERS-1 mission completed a one-year geodetic mapping phase. The combined ERS-1 and GEOSAT mappings provided a major improvement in gravity field accuracy and resolution (Andersen and Knudsen 1998; Cazenave et al. 1996; Hwang and Parsons 1996; Sandwell and Smith 1997; Tapley and Kim 2001) that prompted a second revolution in our understanding of the tectonics of the deep oceans (e.g., Müller et al. 1997; Sandwell et al. 2006; Wessel 2001). The next significant improvement came from a more precise analysis of the raw radar waveforms from ERS-1 and GEOSAT (Maus et al. 1998; Sandwell and Smith 2005). The two-pass waveform retracking approach led to a factor of 1.5 improvement in the accuracy of the marine gravity field that revealed the segmentation of the seafloor spreading ridges as well as a partial mapping of the abyssal fabric on the slow spreading ridges where abyssal relief can exceed 1000 m. In addition, the improved gravity models also revealed thousands of previously uncharted seamounts (Wessel 2001).

Jason-1 and CryoSat-2: Over the past six years, two new satellite altimeters have provided a dramatically improved view of the tectonics of the deep ocean floor (Sandwell et al. 2014). Most of the new information comes from the CryoSat-2 satellite launched by the European Space Agency in 2010. CryoSat-2 has routinely collected altimetry data over ice, land, and oceans since July 2010
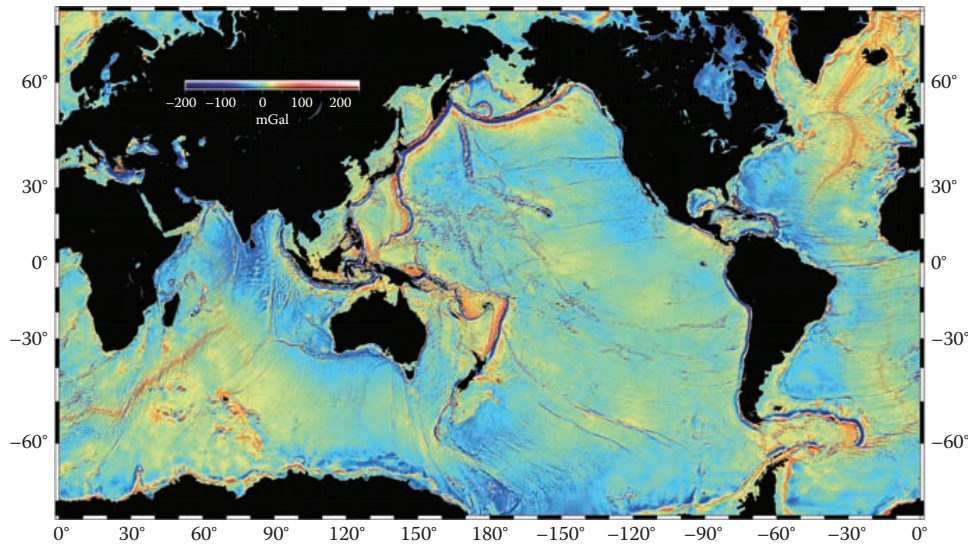
FIGURE 16.1   Gravity anomaly in milligal from GEOSAT, ERS-1, Envisat, Jason-1, and Cryosat-2 radar altimetry. Grid is available at: ftp://topex.ucsd.edu/pub/global_grav_1min

(Wingham et al. 2006). The satellite has a long, 369-day repeat cycle resulting in an average groundtrack spacing of 3.5 km at the equator. To date, it has completed more than six geodetic mappings of the ocean surface. These data are augmented by a complete 14-month geodetic mapping of the ocean surface by Jason-1 from its lower inclination orbit of 66° that compliments the higher inclination orbit CryoSat-2 (88°); the lower inclination provides more accurate recovery of the east-west sea surface slope, especially at low latitudes. The most recent global marine gravity anomaly map (Figure 16.1) based on all of these geodetic mission data with two-pass retracking for optimal range precision (Garcia et al. 2014) has an accuracy that is two times better than the maps derived from GEOSAT and ERS-1.

16.2.2   Methodology and Limitations

Radar altimeters measure the topography of the ocean surface, which is nearly an equipotential surface of the Earth called the geoid. Geoid height, *N*, is the deviation in the shape of the Earth from an ellipsoidal shape defined by the WGS84 ellipsoid. Typical variations in geoid height are ± 33 m whereas variations in ocean surface height due to currents, and eddies are ± 1 m. At the horizontal length scales of interest for seafloor mapping of less than 50 km, geoid height variations dominate the sub-mesoscale oceanographic signals except in areas of high mesoscale variability, such as the eastward extension of the Gulf Stream. In these areas, we rely on temporal averaging to reduce the oceanographic noise. We enhance these small-spatial scale signals in geoid by taking first and second horizontal derivatives. This also provides us with gravity anomaly and vertical gravity gradient, respectively. Let $\Phi(x,y,z)$ be the anomalous gravitational potential as a function of a local Cartesian coordinate system where *z* is up. Variations in potential cause in bumps in the geoid height through Brun's formula (Heiskanen and Moritz 1967)

$$N(x,y) = \frac{\Phi(x,y,0)}{g}$$

where *g* is the average local acceleration of gravity (approximately 9.8 ms²). A positive potential anomaly produces a positive geoid height because for the ocean surface to remain at an equipotential

it must be displaced away from the center of the Earth to a lower potential to offset the local high in the potential. For the areas on and above the ocean surface, the anomalous potential satisfies Laplace's equation.

$$\frac{\partial^2 \Phi}{\partial x^2} + \frac{\partial^2 \Phi}{\partial y^2} + \frac{\partial^2 \Phi}{\partial z^2} = 0$$

The gravity anomaly is the first vertical derivative of the potential anomaly, so $\Delta g = -\frac{\partial \phi}{\partial z}$ and the vertical gravity gradient (VGG) is $\frac{\partial \Delta g}{\partial z} = -\frac{\partial^2 \phi}{\partial z^2}$. Therefore, using Laplace's equation and Brun's formula, it is clear that the VGG is the curvature of the ocean surface

$$\frac{\partial \Delta g}{\partial z} = g\left(\frac{\partial^2 N}{\partial x^2} + \frac{\partial^2 N}{\partial y^2} \right)$$

There is a similar relationship between gravity anomaly and first horizontal derivatives of the geoid that is more easily derived in the Fourier transform domain (Haxby et al. 1983). Note that both the gravity anomaly and the VGG require that the geoid or sea surface height is resolved in both horizontal dimensions. This requires complete altimeter coverage of the surface. Moreover, the errors in the gravity and VGG are smaller when the altimeter tracks are more orthogonal.

For our investigation of seafloor tectonics, we use Laplace's equation in spherical coordinates at wavelengths longer than 20 km and in Cartesian coordinates at shorter wavelengths to construct the gravity anomaly and vertical gravity gradient. Because we are not interested in constructing the geoid, we perform the first derivative directly on the raw altimeter profiles. These along-track slopes are combined in a biharmonic spline analysis to construct east and north grids of sea surface slope (e.g., Sandwell and Smith 2009). As discussed in Olgiati et al. (1995), there are significant computational and accuracy benefits to constructing gravity from along-track slopes rather than first constructing a geoid model and then differentiating to obtain gravity. Moreover, factors that affect the absolute height accuracy of altimetric sea level—such as radial orbit error, ionosphere/troposphere delays and deep ocean tides (Chelton et al. 2001)—have correlation scales long enough that they yield negligible error (1 microradian) in along-track slope (Sandwell and Smith 2009). For gravity recovery at length scales less than 50 km, the remaining important error sources are coastal tide model errors, sub-mesoscale variability, and atmospheric fronts with sharp variations in wet tropospheric delay. We rely on averaging over several mapping cycles to reduce the noise of these sources. As shown previously, the second vertical derivative of the geoid, called the vertical gravity gradient, is simply equal to the curvature of the ocean surface through Laplace's equation. Therefore, computation of VGG is a local operation that does not suffer from the coastal Fourier edge effects that occur when computing vertical gravity from the sea surface slope.

We emphasize that taking the first derivative of the geoid to form gravity anomaly enhances the short wavelength tectonic signals of interest. Moreover, the second derivative needed to form the VGG further enhances the shortest wavelengths, but it also enhances the short wavelength altimeter noise. The error budget for recovery of gravity anomaly and especially VGG is dominated by the range precision of the radar measurement. The main source of environmental noise is the roughness of the ocean surface due to ocean waves. Also note that the amplitude of the gravity signal

decreases exponentially with decreasing wavelength for wavelengths smaller than the mean ocean depth. Therefore, a factor of two improvement in the spatial resolution requires a factor of four reduction in altimeter noise. This can either be achieved by improved radar technology or by repeating the measurement 16 times.

16.2.3 Improved Radar Technology—Current and Future

The most important contribution of the new altimeters (Jason-1 and CryoSat-2) is related to a 1.25 times improvement in range precision with respect to the older altimeters (ERS-1 and GEOSAT) (Garcia et al. 2014). The newer altimeters have pulse repetition frequencies (PRFs) of 1950 Hz and 2060 Hz, respectively, while the older instruments were technologically limited to lower values of 1020 Hz. Theoretically, this approximate doubling of PRF should result in a square root of two improvement in range precision; the actual improvement is somewhat smaller (1.25) perhaps reflecting the onset of echo correlation at the 2 kHz PRF. Nevertheless, this improvement in range precision maps directly into an improvement in gravity field accuracy.

CryoSat-2 was also operated in a new Synthetic Aperture Radar (SAR) mode over very limited areas of the oceans. This mode has a much higher PRF of 18.2 kHz, and the highly correlated echoes are summed coherently in bursts of 64 pulses to form a long synthetic aperture. This enhances along-track resolution in the form of a set of narrow beams distributed in the along-track direction (Wingham et al. 2006). Unlike the conventional pulse-width limited geometry, the resulting echo waveforms have useful information in both the leading and trailing edges. This, together with an increase in the effective number of independent samples resulting from the SAR technique, reduces the height noise by a factor of approximately 1.4 compared to conventional altimeters. Comparison of height noise performance indeed shows this expected improvement for CryoSat-2's SAR, but similar gains for pulse-width limited echoes are obtained by a two-pass processing scheme in which the slowly varying ocean wave height is first estimated and smoothed and then excluded from the estimation process in the second pass (Garcia et al. 2014).

There are two technological developments that will further improve the altimeter range precision. The first is a new shorter wavelength altimeter called AltiKa aboard the SARAL spacecraft launched by the Indian Space Research Organization (ISRO) and French space agency, Centre National d'Etudes Spatiales (CNES), in 2013. Recent studies show that the range precision of AltiKa is two times better than Ku-band altimeters operated in non-SAR mode (e.g., Jason-1 and Cryosat-2 low resolution mode, or LRM) (Smith 2015; Zhang and Sandwell 2016). In July 2016, the orbit of SARAL/AltiKa was changed from the 35-day repeat trackline of ERS and Envisat to a new non-repeat geodetic mission. There will be another major improvement in the accuracy of the gravity field if it survives for 1.3 years to obtain complete coverage. The second technology is a planned swath altimeter mission called Surface Water and Ocean Topography (SWOT) scheduled for launch in 2021. Engineering estimates of range precision are up to a factor of five times better than the current altimeters, so one can expect another significant boost in resolution in 2025.

The remainder of this chapter is focused on the imaging of small-scale tectonics in the deep oceans and continental margins using mainly maps of VGG, especially in areas with enigmatic, poorly understood seafloor tectonic fabric such as seen in the Java Sea (Figure 16.2). The curved lineaments shown here were recently discussed by Zahirovic et al. (2016), who proposed that they may reflect successive generations of volcanic arcs that are now curved because of oroclinal bending in a compressional episode driven by the rotation of Borneo. We also note that marine gravity has many other applications, such as inertial guidance of moving platforms, planning shipboard surveys, petroleum exploration, estimating the strength of the lithosphere, and searching for meteorite impacts on the ocean floor. The gravity is also used for predicting seafloor bathymetry in uncharted areas.
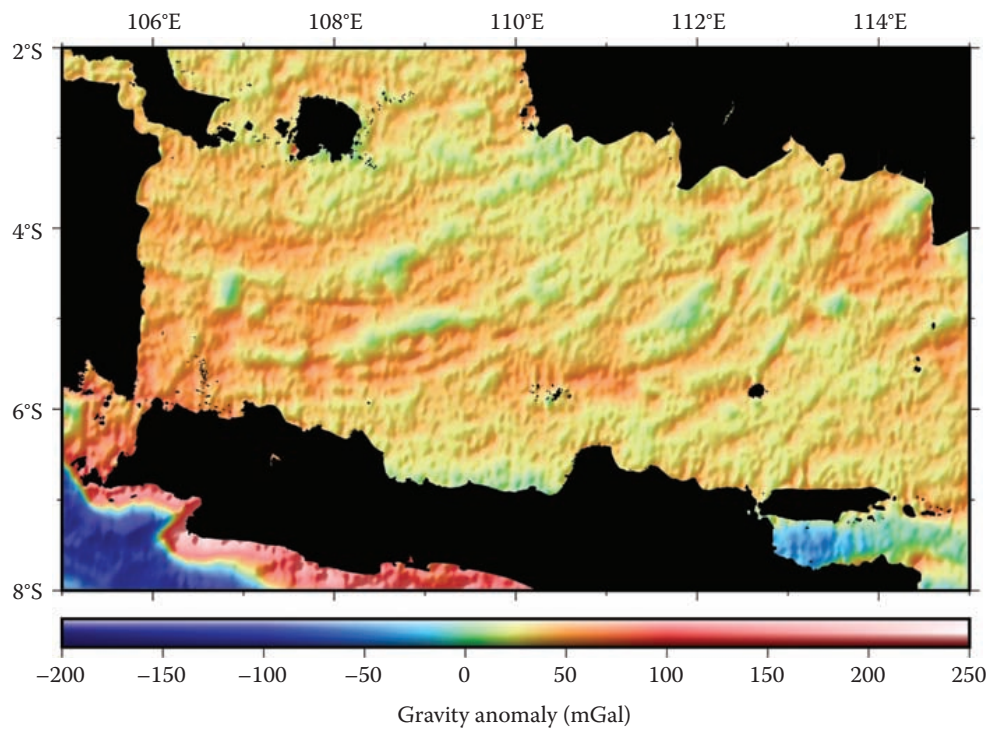
(a)
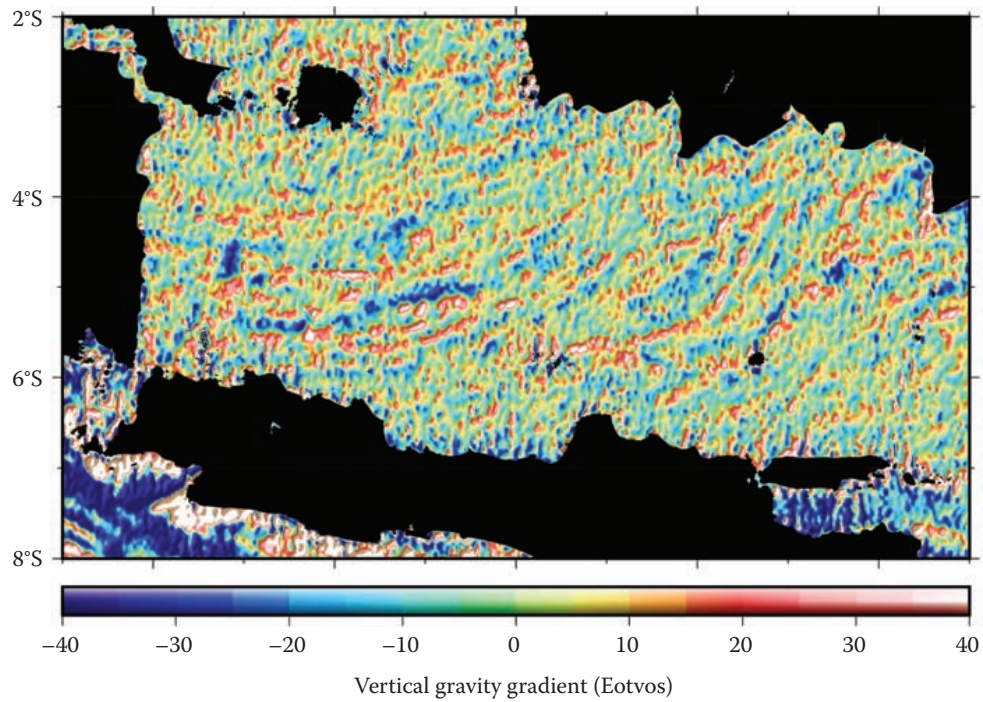
(b)

FIGURE 16.2   Gravity anomaly of the Java Sea (a). Vertical gravity gradient (VGG) of Java Sea reveals small-scale anomalies related to basement structure (b).

16.3   OCEANIC MICROPLATES

Oceanic microplates are small and independently rotating rigid plates that form at spreading centers, either between two plates or at a triple junction, due to ridges propagating into, and capturing fragments of, existing oceanic lithosphere. They proceed to grow due to accretion at the new spreading center. Based on our knowledge from well-mapped microplates, they range in size from only a couple of thousand to more than 1.2×10^6 km^2 in area and are active for less than a few million years to around 10 million years. Although microplates are short-lived, transient features, they are an important record of spreading center reorganization and periods of asymmetric lithospheric accretion. Microplate formation at spreading ridges has almost exclusively been studied in the Pacific, particularly in the eastern Pacific, for more than 40 years. Here, there are several actively forming microplates (e.g., Easter, Juan Fernandez, Galapagos, North Galapagos) and many extinct Cenozoic ones that have since been detached from an active spreading ridge (e.g., Mathematician, Bauer, Friday, Selkirk, Hudson) (Figure 16.3), enabling their formation and associated seafloor structures to be studied in depth. Yet the recent discovery of a microplate in the Indian Ocean, based on advances in seafloor imaging using satellite altimetry, now enables the study of microplate formation outside of the Pacific to gain a broader understanding of where and how these structures develop (Matthews et al. 2016).

16.3.1   MODELS FOR MICROPLATE FORMATION

In the wake of the pioneering work of Hey and colleagues on propagating rifts (e.g., Hey 1977; Hey et al. 1980), the origins and mechanisms of microplate formation received considerable attention, particularly in the 1980s and 1990s, as ship-derived geophysical data sets enabling mapping along the East Pacific Rise expanded (see Searle 2013, for a review). The pivotal "edge-driven" model of microplate formation, presented by Schouten et al. (1993), focuses on the growth of established microplates and has since been frequently adopted and modified. According to Schouten et al.'s (1993) "edge-driven" model of microplate formation, rotation is driven by the drag of the bounding plates and is analogous to the motion of a gear or roller bearing between two pieces of wood that are sliding past each other. An important aspect of the model is that the microplate has two axes of rotation located at each of its margins with the neighboring plates, and these are no-slip boundaries. Furthermore, the microplate is assumed to be rigid, with deformation confined to its edges.

Bird and Naar (1994) presented a model for microplate formation based on their investigation of the Easter and Juan Fernandez microplates. In their model, microplate formation is linked with rift propagation from transform faults, possibly at intratransform spreading centers. The microplate forms between the existing spreading ridge and the propagating ridge. One spreading axis eventually dies, leading to microplate detachment. Bird and Naar (1994) recognized that a number of factors may facilitate rift propagation from the transform fault. For instance, warmer lithospheric temperatures may reduce the effective lithospheric thickness difference across the intratransform region; warm and young lithosphere, such as at an intratransform spreading center, is more likely to concentrate stress and crack; and finally, excess relief due to the excess melt supply at an intratransform spreading center may be a driving force for ridge propagation (Phipps Morgan and Parmentier 1985).

Eakins (2002) built on the models of Schouten et al. (1993) and Bird and Naar (1994), based on studying formation of the Bauer and Hudson microplates from high-resolution ship-track data. In his model for microplate initiation and growth, microplates form when coupling increases across a free slip boundary, such as a transform. This increased coupling leads to tearing of one or both plates and the initiation of a propagator. As the propagator grows, the microplate core rotates as it is dragged by the adjacent plates. This initial increase in shear coupling across a previously free-slipping boundary could be caused by plate motion changes that either lead to transtension (Bird and Naar 1994) or transpression. According to Eakins (2002), propagation from an intratransform spreading center is not necessary but may facilitate the process and localize the rifting. Four drivers
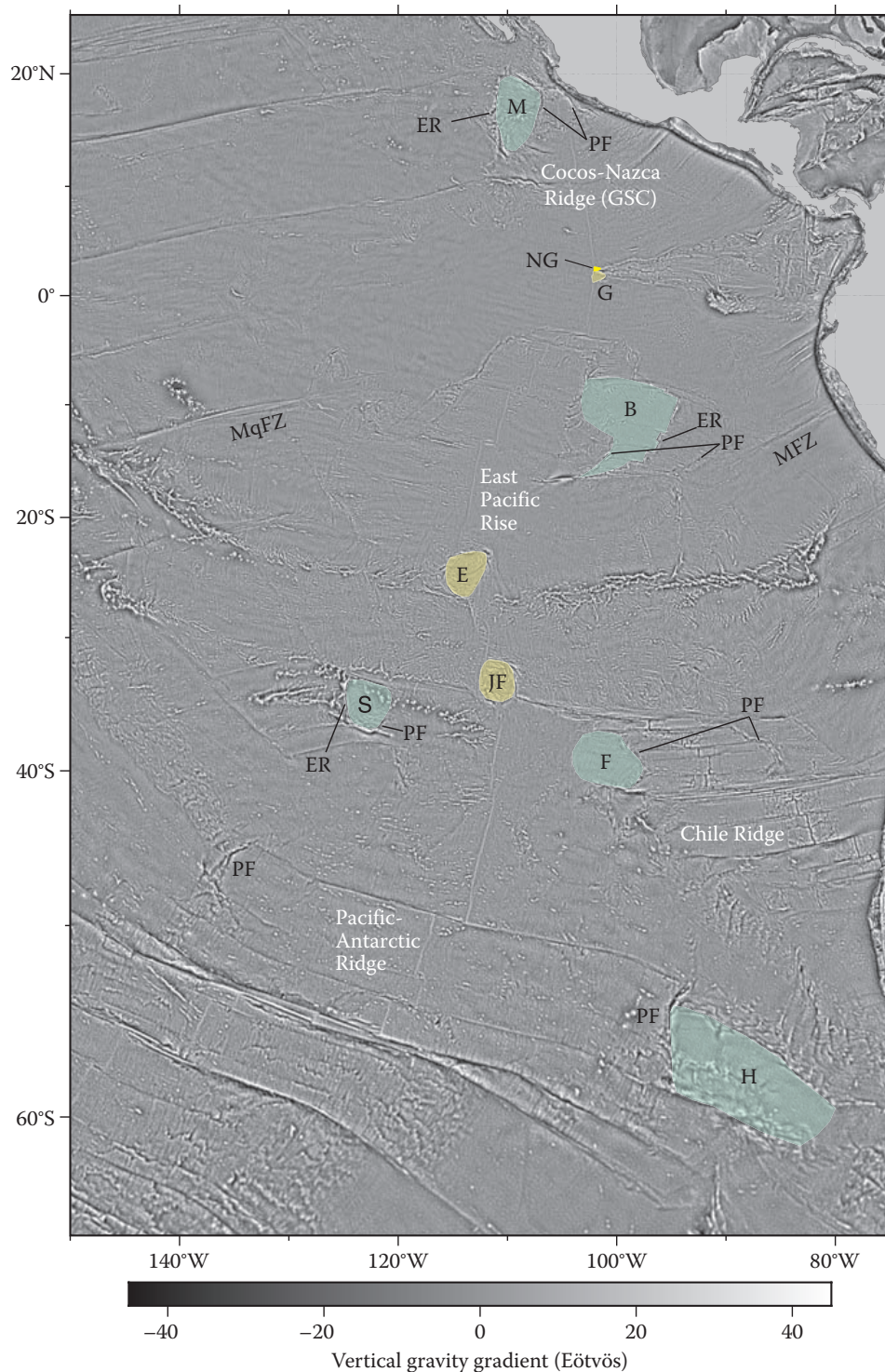
FIGURE 16.3 Pacific vertical gravity gradient map and microplate vertical gravity gradient (VGG) map (Sandwell et al. 2014) of the eastern Pacific Ocean basin showing active (yellow) and extinct microplates (green). The Pacific–Antarctic Ridge and East Pacific Rise produce positive VGG anomalies, while the Chile Ridge produces a negative VGG anomaly. Examples of the pseudo faults (PF) and extinct ridges (ER) associated with the extinct microplates are highlighted. B, Bauer Microplate; E, Easter Microplate; F, Friday Microplate; G, Galapagos Microplate; GSC, Galapagos Spreading Centre; H, Hudson Microplate; JF, Juan Fernandez Microplate; M, Mathematician Microplate; MFZ, Mendaña Fracture Zone; MqFZ, Marquesas Fracture Zone; NG, North Galapagos Microplate; S, Selkirk Microplate.

and/or facilitators of microplate formation are currently recognized that can occur in combination with each other. These include plate reorganizations, hotspot activity, fast spreading, and triple junction migration (Hey 2004).

16.3.2 ASSOCIATED SEAFLOOR STRUCTURES

Microplates are associated with oblique seafloor structures rather than those parallel or perpendicular to the direction of spreading prior to ridge propagation (Hey 2004). For example, due to their independent rotation, fan-shaped patterns of isochrons and rotated abyssal hills are characteristic features (Eakins 2002; Hey 2004; Hey et al. 1988; Mammerickx et al. 1988). Ridge propagation during microplate formation produces a pair of pseudo faults, which are linear boundaries between the young lithosphere accreted at the new ridge and the older preexisting lithosphere. Pseudo faults are often mirror images of each other, although microplate rotation reduces this symmetry (Tebbens and Cande 1997). If spreading ceases at one of the microplate boundaries, then an extinct ridge will be left behind (Figure 16.4).
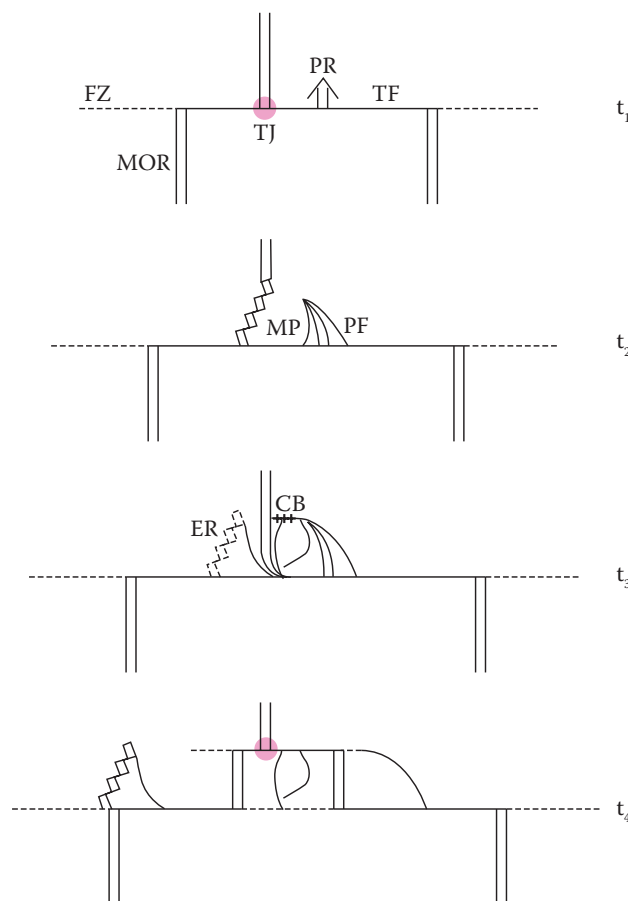
FIGURE 16.4 Microplate formation and triple junction migration. Bird et al.'s (1999) model for microplate formation associated with triple junction migration as has been observed in the Pacific. The model begins with a new ridge propagating from a transform fault at the ridge-transform-transform triple junction (t_1). The microplate forms between the propagating ridge and the preexisting triple junction ridge (t_{2-3}). Once the transform fault that forms the southern boundary of the microplate "freezes," the microplate detaches (t_4). In this particular model, the triple junction migrates northward and the microplate attaches to the southern plate at the triple junction. However, the ridge can propagate into any of the three plates at the triple junction. The triple junction (highlighted pink) is only present during t_1 and t_4. (Adapted from Figure 16.3 of Bird, R.T., et al., *Geology*, 27(10), 911–914, 1999.)

16.3.3 Recent Advances in Mapping the Structure and History of Microplates using Satellite Altimetry

Seafloor structures that are produced during microplate formation have typically been mapped using ship-track data sets, yet the larger structures such as pseudo faults, extinct ridges, and sometimes abyssal hills can also be illuminated in satellite altimetry-derived gravity maps of the seafloor, which provide a proxy for seafloor topography. In particular, VGG data better resolve short-wavelength linear tectonic structures compared to free-air gravity data, and the recent near-global VGG data set of Sandwell et al. (2014) can resolve features as small as 6 km in width. Improvements in satellite data not only reveal new structures on the seafloor but also confirm the identification of features that were previously only poorly resolved and thus uncertain.

16.3.3.1 Indian Ocean

The mapping of seafloor tectonic fabric in the Indian Ocean using the VGG data set of Sandwell et al. (2014) recently led to the discovery of the approximately 47-Ma Mammerickx Microplate (Figure 16.5), an extinct microplate west of the Ninetyeast Ridge, centered on approximately 83°E and 21.5°S (Matthews et al. 2016). Prior to this study, remnants of a system of dual spreading and ridge rotation associated with Pacific-style microplate formation had not yet been clearly identified in the Indian or Atlantic oceans. The Mammerickx Microplate is bounded in the north by an extinct ridge and in the south by a pseudo fault, indicating that microplate formation occurred during a southward relocation of the Antarctic-Indian spreading ridge that isolated a fragment of the Antarctic Plate (Figure 16.5b). The conjugate pseudo fault to that which forms the southern boundary of the microplate is located on the Antarctic Plate, centered on 65°E and 41°S to the north of the Kerguelen Plateau (Figure 16.5a). These pseudo faults were produced during rapid (likely less
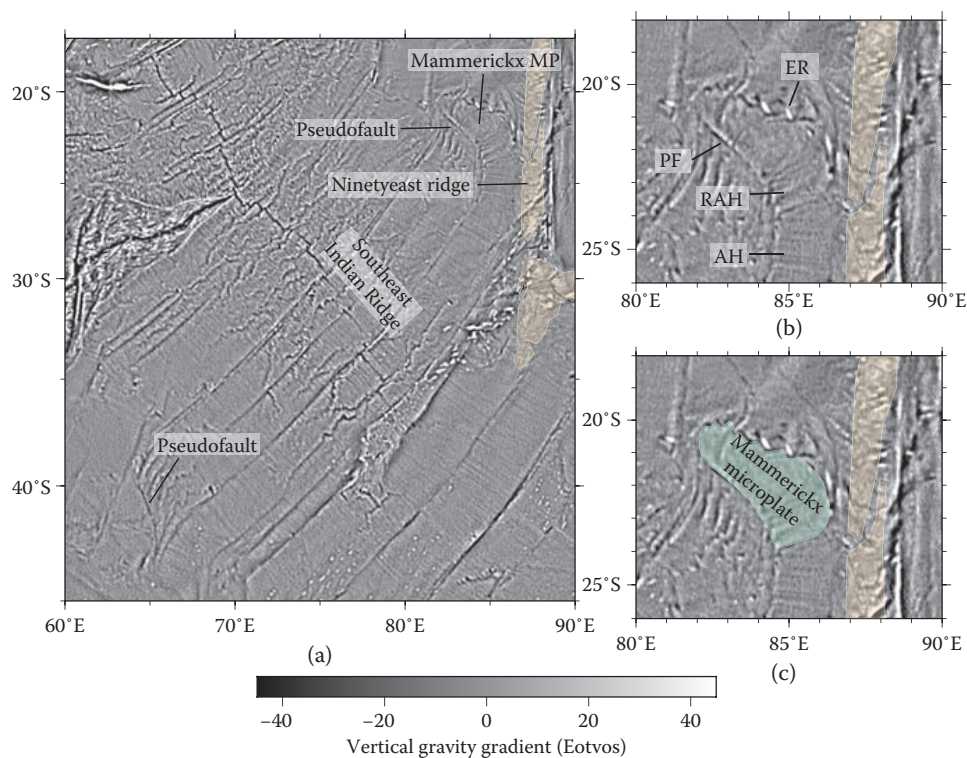
FIGURE 16.5 (a–c) Mammerickx Microplate, Indian Ocean. Vertical gravity gradient (VGG) maps (Sandwell et al. 2014) of the Indian Ocean showing the Mammerickx Microplate and associated structures. Large igneous provinces are shaded orange (Whittaker et al. 2015). AH, abyssal hills; ER, extinct ridge; MP, microplate; PF, pseudo fault; RAH, rotated abyssal hills.

than 2 million years) westward ridge propagation from a developing transform fault (Matthews et al. 2016). Independent microplate rotation is indicated by a slight asymmetry in the pseudo fault pair, as well as counterclockwise rotated abyssal hill fabric that formed during rotation and southward growth of the dying spreading ridge, which was also confirmed by ship-track bathymetry data. Matthews et al. (2016) provided a detailed review of the potential driving mechanisms for the formation of the microplate and proposed that it was likely triggered by a plate reorganization, namely India-Eurasia collision, and fast spreading and hotspot activity, which had been present for tens of millions of years in the region, facilitated the event by contributing to the production of warm, thin, and weak lithosphere. The use of satellite gravity data, with the highest resolution yet published (Sandwell et al. 2014), to map microplate structures is methodologically significant (Goff and Cochran 1996) as typically these structures have been investigated using expensive ship-track data.

16.3.3.2 Pacific Ocean

The central Pacific region is characterized by extremely fast full spreading rates between the Pacific and Nazca plates, which rose from about 10 cm/y to more than 17 cm/y in the mid-late Cenozoic between magnetic chrons 18 (40 Ma) and 5 (11 Ma) north of the Chile Fracture zone (Wright et al. 2016). Such fast spreading rates are known to facilitate ridge propagation and microplate formation as they produce a wide region of hot, relatively thin lithosphere along the spreading ridge and enhance stress changes along the ridge (Hey 2004; Hey et al. 1985). The spreading asymmetry analysis by Wright et al. (2016) indicates large asymmetries in the spreading corridor east of the Juan Fernandez Microplate (Figure 16.6), with about 55% to 60% of the crust generated at the mid-ocean
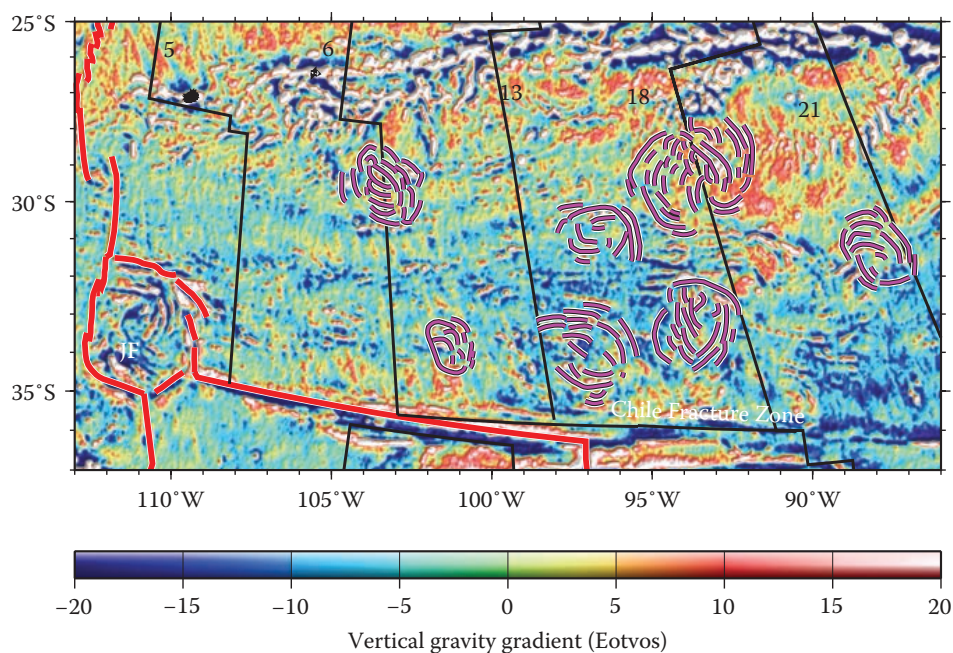
FIGURE 16.6 Paleo-Microplates in the Central Pacific Ocean. Vertical gravity gradient (VGG) map (Sandwell et al. 2014) of the spreading corridor east of the Juan Fernandez (JF) microplate and north of the Chile Fracture Zone. Current plate boundaries are outlined in red. VGG anomalies, outlined in magenta, illustrate the location of nine paleo-microplates. Their fabric has been interpreted by following the troughs of associated negative VGG anomalies. Schematic seafloor isochrons are shown for Chrons 5 (11 Ma), 6 (20 Ma), 13 (33 Ma), 18 (39 Ma), and 21 (48 Ma) (Wright et al. 2016) to provide rough age estimates for the tectonic stages when these microplates were active. Note the curved seafloor fabric indicative of microplate rotation and the narrow, partly curved VGG highs, likely corresponding to compressional ridges, as mapped around the Easter Microplate (Rusby and Searle 1993).

ridge left on the Nazca Plate. In this region, the VGG data set of Sandwell et al. (2014) reveals previously unmapped paleo-microplates and confirms the existence of several paleo-microplates that were identified by Matthews et al. (2011) using an older version of the VGG data (Sandwell and Smith 2009). The extinct microplates are clearly visible through the curved lineations caused by their rotation, driven by the drag of the Nazca and Pacific plates, akin to that proposed for the Easter Microplate (Schouten et al. 1993) (Figure 16.6). After their formation and a period of rotation between a propagating and a receding ridge tip (Hey 2004), they were all eventually accreted to the Nazca Plate. The identification of these paleo-microplates is not only based on the curved seafloor fabric they have left behind due to their rotation history about stage poles proximal to their center but also on curved compressional ridges, which are expressed as narrow VGG highs (Figure 16.6). Compressional brittle deformation of the crust within microplates has been well documented for the Easter Microplate (Rusby and Searle 1993). Here, narrow ridges, up to 1 km high, have been shown to be associated with thin-skinned thrusting in response to local changes in the stress field (Rusby and Searle 1993). These features are preserved on old ocean crust and stand out among the background abyssal hill fabric (Figure 16.6). The apparent ubiquity of paleo-microplates in this spreading corridor may indicate that they were not driven by a major plate reorganization, as has been inferred for the formation for the Easter and Juan Fernandez microplates (Bird and Naar 1994), because there is no evidence for frequent plate reorganizations between the Nazca and Pacific Plates during the period of their formation (i.e., since approximately 50 Ma) (Wright et al. 2016). Instead they appear to be mainly driven by ultrafast spreading rates.

16.4 MAPPING MAJOR TECTONIC EVENTS IN THE OCEAN BASINS

Tectonic structures that are produced at mid-ocean ridges as a result of seafloor spreading, such as fracture zones, abyssal hills, propagating ridges and microplates, provide direct constraints on the direction and/or speed of relative plate motions. When combined with crustal age data, these structures allow for the construction of robust plate reconstruction models. Fracture zones and abyssal hills, the most pervasive structures on the seafloor, are particularly valuable for charting the motion of the plates. Their orientation records the direction of plate motion, and their morphologies and spacing can indicate the nature of the spreading regime, such as whether it was ultra-fast, fast, intermediate, slow, or ultra-slow (e.g., Sandwell and Smith 2009).

   Patterns in the spatial distribution of structures that originate at spreading ridges, along with the occurrence of fracture zone bends and sudden changes in fracture zone morphology, also reveal evidence for plate reorganizations, including reorientations, relocations, or changes in segmentation of divergent plate boundaries and plate motion changes. Although continents are also sensitive to plate reorganizations, compared to the oceanic realms, they are more affected by deformation, tectonic overprinting, and erosional processes, all of which make it more difficult to unambiguously attribute continental structures and events to plate reorganizations. Therefore, seafloor fabric indicators of plate reorganizations are crucial for their identification and analysis. An enormous volume of work has focused on the Eocene global tectonic reorganization, about approximately 50 Ma in age, and recently reviewed in Müller et al. (2016). Here, we focus particularly on the controversial mid-Cretaceous (approximately 105–100 Ma) reorganization and review to what extent satellite gravity data, combined with other marine geophysical and geological data sets, are contributing to an improved understanding of the structural expression, age, and regional occurrence of this event.

16.4.1 THE ENIGMATIC MID-CRETACEOUS TECTONIC EVENT

A mid-Cretaceous (approximately 100 Ma) spreading reorganization in the Indian Ocean was originally proposed by Powell et al. (1988). The now well-mapped associated seafloor fabric illustrates that this event produced one of the most prominent suites of fracture zone bends on Earth, in the Wharton Basin west of Australia, that are now well-resolved in satellite free-air and vertical gravity
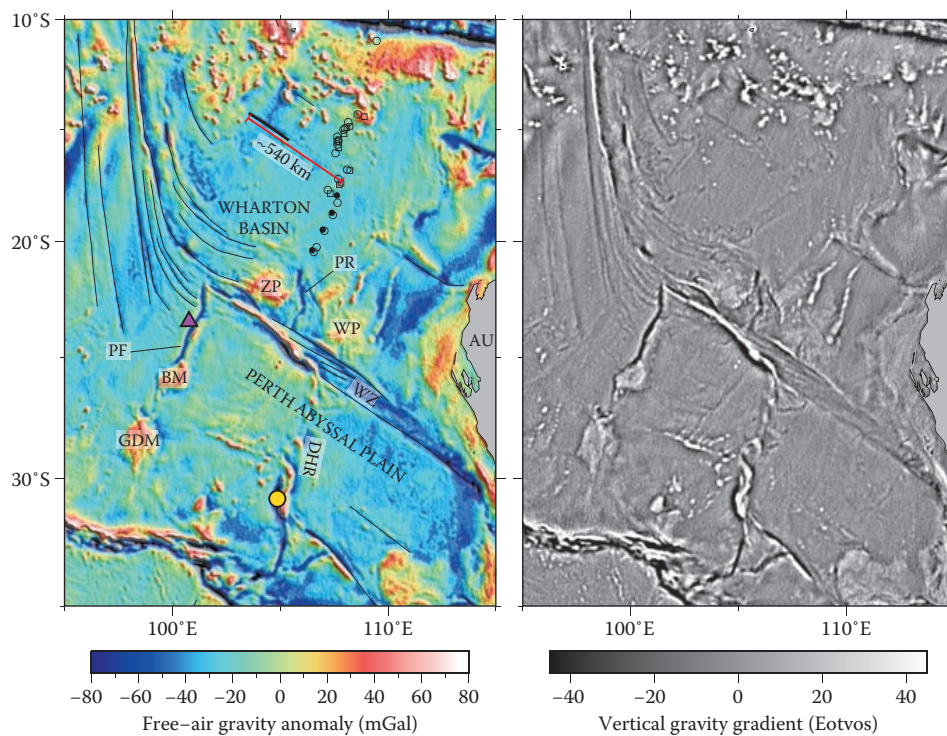
FIGURE 16.7   Wharton Basin Gravity Anomaly Maps. Free-air gravity (a) and vertical gravity gradient (VGG; b) maps of the Wharton Basin and Perth Abyssal Plain to the west of Australia (AU) (Sandwell et al. 2014). Fracture zones are represented by thin black lines, although a single fracture zone in the Wharton Basin that is discussed in the text is drawn as a thick black line (Wessel et al. 2015). M0 magnetic anomaly picks in the Wharton Basin are from Müller et al. (1998) (squares), Ségoufin et al. (2004) (hollow circles), and Gibbons et al. (2013) (filled circles). DSDP Site 256 is a purple triangle, and dredge site 5 from Whittaker et al. (2016) is a yellow circle. BM, Batavia Microcontinent; DHR, Dirck Hartog Ridge; GDM, Gulden Draak Microcontinent; PF, pseudo fault; PR, extinct propagating ridge feature; WP, Wallaby Plateau; WZ, Wallaby-Zenith Fracture Zone; ZP, Zenith Plateau.

gradient data sets (Figure 16.7). These fracture zone bends express an approximately 50° clockwise change in the direction of spreading between Australia and India. Other events reported to have been concomitant with formation of the Wharton Basin fracture zone bends include a minor change in the direction of spreading between Africa and Antarctica, which produced broad fracture zone bends to the southwest of Madagascar and off the Queen Maud Land margin of Antarctica (Bernard et al. 2005), and a change in the direction of spreading between Antarctica and India that produced fracture zone bends in the Enderby Basin and the Bay of Bengal (Rotstein et al. 2001). Veevers (2000) reviewed the mid-Cretaceous event in a wider spatial context and showed that a series of tectonic and stratigraphic regime changes in Australia, New Zealand, and the Pacific Rim, and bends in Pacific hotspot trails that indicate a swerve of the Pacific Plate, also occurred in the mid-Cretaceous at about 100 Ma. Most of this work predated the use of detailed satellite altimetry-derived gravity anomalies to map seafloor structures associated with this event.

Matthews et al. (2012) produced the first detailed interpretation of changes in seafloor fabric that occurred from approximately 110–90 Ma, based on satellite gravity data. They concluded that the reorganization was likely global in scale and initiated at approximately 105–100 Ma. This was based on the widespread occurrence of prominent fracture zone bends (Wharton Basin, Enderby Basin, Bay of Bengal, Weddell Sea, South Atlantic) and fracture zone terminations (Central and South Atlantic) in the Indian and Atlantic oceans (Figure 16.8) and hotspot trail bends in the Pacific, as noted by Veevers (2000). Unfortunately, seafloor structures that form at approximately 105–100 Ma
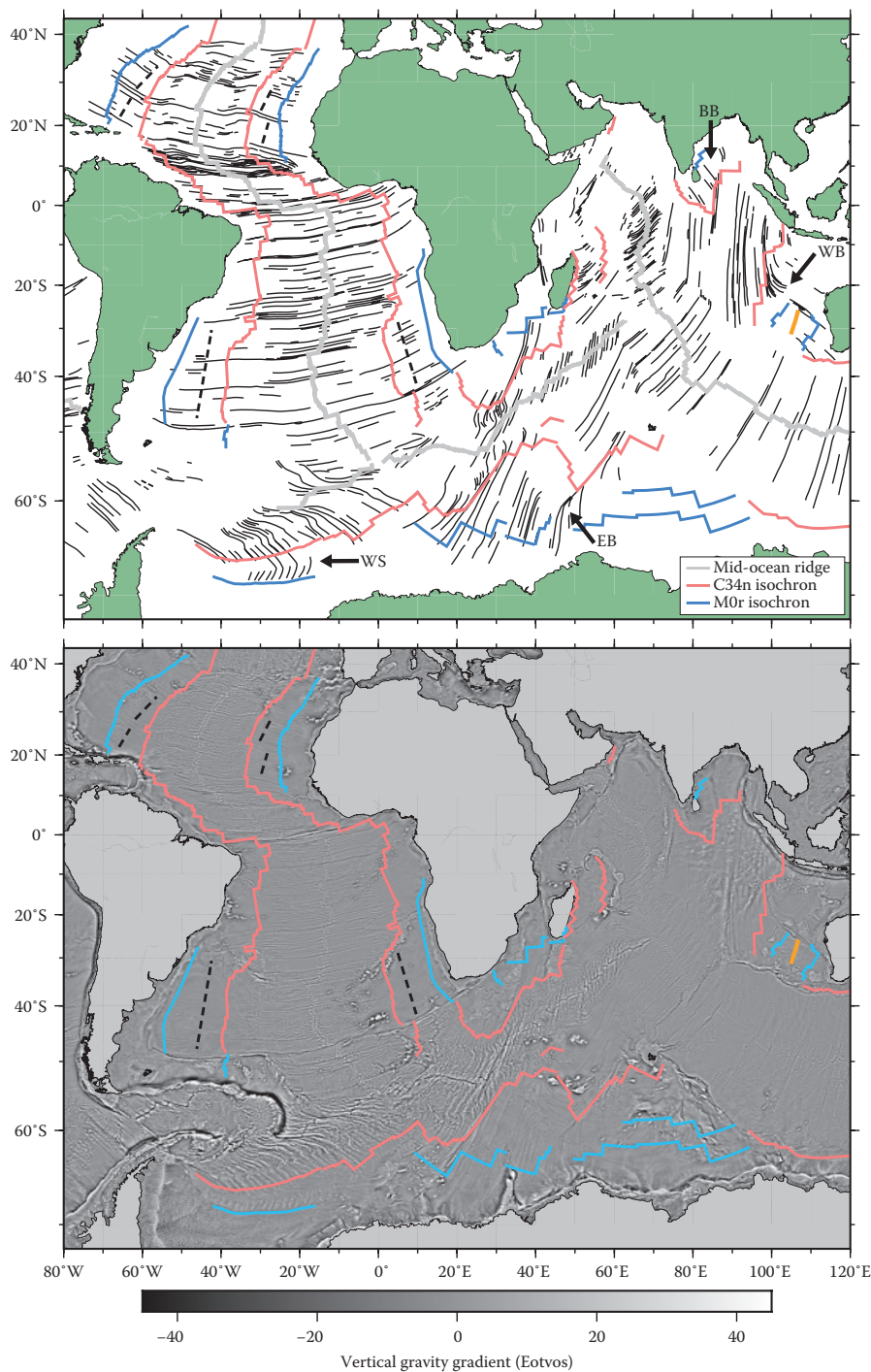
FIGURE 16.8 Tectonic Fabric of The Atlantic and Indian Oceans. Seafloor fabric map of the Atlantic and Indian oceans showing fracture zones (black lines) and mid-ocean ridges (bold gray lines) (a). Arrows point to the fracture zone bends in the Weddell Sea (WS), Enderby Basin (EB), Bay of Bengal (BB), and Wharton Basin (WB), and a dashed line demarcates the change in seafloor fabric of the Central and South Atlantic, from rougher to smoother (Matthews et al. 2012). Seafloor that formed during the Cretaceous Normal Superchron is bounded by the C34n (83 Ma, young end) and M0r (120.6 Ma, young end) isochrons of Seton et al. (in prep). Fracture zones are from Wessel et al. (2015), and mid-ocean ridges are from Sandwell and Smith (2009). The extinct Dirck Hartog Ridge in the Perth Abyssal Plain, to the southeast of the Wharton Basin fracture zone bends, is plotted as an orange line (Whittaker et al. 2016). A vertical gravity gradient (VGG) map of the region (Sandwell et al. 2014) is also provided (b), in which the aforementioned seafloor tectonic structures can be identified.

are difficult to date as they coincide with the Cretaceous Normal Superchron (CNS), a prolonged period (approximately 37 million years) of stable magnetic field polarity. Matthews et al. (2012) therefore used absolute ages from ocean drilling data where available (Wharton Basin and Central Atlantic), along with extrapolations of published pre- and post-CNS spreading rates to estimate the ages of the seafloor structures they identified in the Indian and Atlantic oceans within CNS seafloor. They assigned an age of 104 Ma to the spreading reorganization that produced the major fracture zone bends in the Wharton Basin, 98 Ma to the Antarctica-Indian spreading reorganization, 105 Ma to fracture zone bends in the Weddell Sea, and 101 and 102–96 Ma to increases in spreading rate in the Central and South Atlantic, respectively, that they identified from a decrease in seafloor roughness (see Matthews et al. 2012, Appendix B). Of the different ocean regions, their estimate for the Wharton Basin reorganization was most well constrained as they were able to use four different dating approaches, including the use of a dated DSDP dredge sample in the location of the fracture zone bends (Davies et al. 1974).

To obtain tighter constraints on the tectonic evolution of the eastern Indian Ocean during the mid-Cretaceous, Desa and Ramana (2016) recently reanalyzed ship-track magnetic anomalies in the Wharton Basin, Bay of Bengal, and Enderby Basin, focusing on the identification of reversals within the CNS that have been dated at 92 and 108 Ma (Granot et al. 2012). These internal markers in the CNS were mapped in these regions and led Desa and Ramana (2016) to propose an age of 102 Ma for the spreading reorganizations at the Indian-Australian and Indian-Antarctic ridges.

Despite mounting work in support of a major plate reorganization at about 100 Ma, it was recently proposed by Talwani et al. (2016) that the change in motion of the Indian plate may have initiated in the Early Cretaceous, as early as 118 Ma. This was based on their estimates of the age of the fracture zone bends in the Enderby Basin, the eruption of the Rajmahal and Sylhet traps from the Kerguelen Plume, and the proposal that the reorganization coincided with a northward ridge jump in the Eastern Enderby Basin (Talwani et al. 2016). This ridge jump event isolated the continental Elan Bank and was previously described by Gaina et al. (2007) and Gibbons et al. (2013), although these authors did not link the ridge jump with formation of the fracture zone bends.

Dating the Enderby Basin fracture zone bends is difficult as they formed during the CNS; furthermore, there are no absolute age constraints nearby—for instance, from seafloor dredging or drilling. Talwani et al. (2016) measured the distance between the bend in the Kerguelen Fracture Zone and their new M0 magnetic anomaly pick to the south and, using a spreading rate of 40 mm/y, they arrived at an estimated age of 116.2 Ma for the bend, an age similar to that of the ridge jump and eruption of the Rajmahal and Sylhet traps. However, Talwani et al.'s (2016) interpretation of the M0 magnetic anomaly is greater than 130 km north of the M0 picks of Gaina et al. (2007), specifically their Model 2, which assumes the ridge jump affected the Eastern Enderby Basin and is consistent with the work of Gibbons et al. (2013), who identified a pseudo fault in the Eastern Enderby Basin (Figure 16.9). Furthermore, their M0 magnetic anomaly interpretation in the Western Enderby Basin (east of the Gunnerus Ridge) is 100 km and 140 km north of the interpretations of Eagles and König (2008) and Marks and Tikku (2001), respectively, which are all derived from the same ship data.

16.4.2 Insights from combining satellite altimetry with geological and geophysical ship data

Detailed seafloor fabric observations from satellite altimetry, paired with other marine geophysical data to support a major reorganization in the Indian Ocean, have recently grown to include a major mid-Cretaceous ridge jump (Gibbons et al. 2013; Watson et al. 2016; Williams et al. 2013) in the Perth Abyssal Plain east of the major Wharton Basin fracture zone bends (Figure 16.9). The greater than 500-km-long, roughly north-south trending Dirck Hartog Ridge is an extinct spreading ridge that formed during a westward jump in the Australian-Indian spreading center (Watson et al. 2016). Although the structure has the appearance of an extinct ridge in VGG maps, its classification has
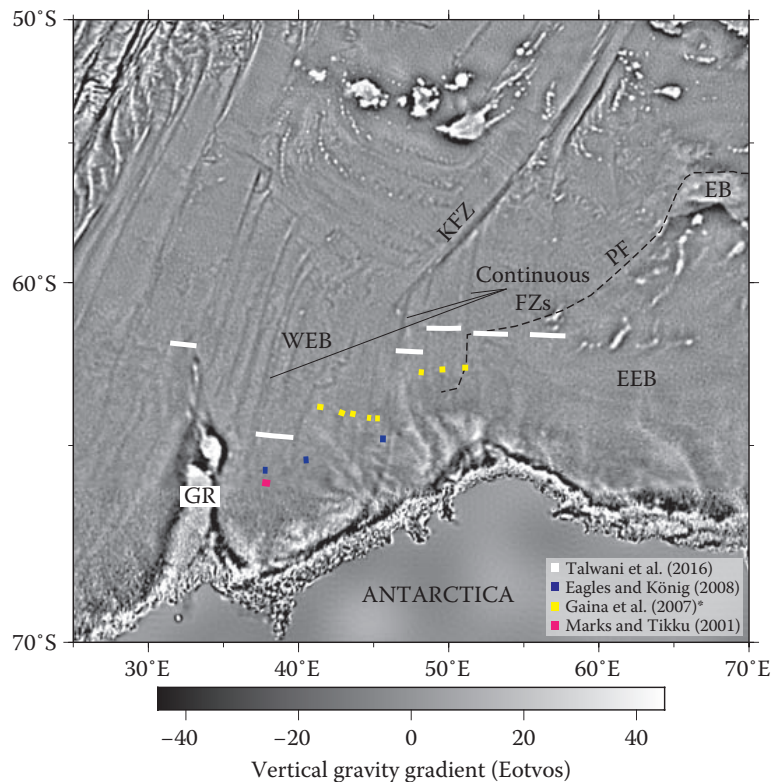
FIGURE 16.9 Vertical gravity gradient of the Enderby basin. Vertical gravity gradient (VGG) map (Sandwell et al. 2014) of the Western (WEB) and Eastern Enderby Basin (EEB) showing the M0r (120.6 Ma, young end) magnetic anomaly identifications of Talwani et al. (2016), Eagles and König (2008), Gaina et al. (2007), and Marks and Tikku (2001). The pseudo fault (PF) identified in the study of Gibbons et al. (2013), which formed during the northward ridge jump that isolated the Elan Bank (EB), is shown as a dashed line. To the west of this boundary, fracture zones are continuous (examples of this are identified in the map), suggesting that spreading was continuous in this corridor and unaffected by the ridge jump. GR, Gunnerus Ridge; KFZ, Kerguelen Fracture Zone.

been confirmed by ship-track magnetic anomaly interpretations (Williams et al. 2013) and detailed analysis of swath bathymetry (Watson et al. 2016). An age of 102.3 ± 2.5 Ma was obtained from $^{40}Ar/^{39}Ar$ dating of a plagioclase crystal in a gabbro sample from the Dirck Hartog Ridge (Whittaker et al. 2016). The ridge jump event resulted in the calving off of two continental fragments (Batavia and Gulden Draak microcontinents) from the Indian passive margin, both of which align with the pseudo fault that formed during ridge propagating (Whittaker et al. 2016) (Figure 16.7). These combined data suggest that a spreading reorganization at approximately 105 Ma caused a ridge jump and subsequent microcontinent formation at approximately 104–101 Ma, immediately prior to the formation of the curved Wharton Basin fracture zones clearly visible in the VGG image (Whittaker et al. 2016) (Figure 16.7). These timings are consistent with the results of Desa and Ramana (2016), who proposed an age of 102 Ma for the ridge jump based on their identification of CNS internal time markers in ship-track magnetic anomaly profiles.

To understand the timing and nature of the Indian Ocean reorganization, one needs to consider events at all of its plate boundaries as a major reorganization at one boundary will affect its other boundaries. Talwani et al. (2016) suggested that the Wharton Basin fracture zone bends (Australian-Indian spreading ridge) could be as old as 117 Ma, forming some time during the period 100–117 Ma. In the Wharton Basin, to the northeast of the fracture zone bends, at least 540 km of quite smooth seafloor was produced between the time of anomaly M0 and the change in seafloor spreading (Figure 16.7). This observation is supported by interpretation of seafloor fabric to the north of the Zenith Plateau, where a well-resolved fracture zone can be identified and the seafloor fabric shows no sign of

ridge extinction or ridge jumps (Matthews et al. 2012). The production of this amount of seafloor and considering a variety of published spreading rates for just prior to M0 (3.5–5.5 cm/y) places an upper limit on the age on the reorganization of approximately 105.2–110.8 Ma (based on the timescale of Gee and Kent 2007). In contrast, Talwani et al. (2016) proposed that measuring the distance between the suite of fracture zone bends and the M0 anomalies may result in an estimate as old as 117 Ma for the reorganization. However, the seafloor to the east of the fracture zone bends, which Talwani et al. (2016) relied upon for their estimates, has been affected by a complex tectonic history including a major ridge jump (Gibbons et al. 2013; Watson et al. 2016; Whittaker et al. 2013; Williams et al. 2013) and possibly aborted ridge propagation in the region between the Zenith and Wallaby plateaus (see VGG image and interpretation in Figure 16.7); therefore, it is not reliable to measure the distance between the bends and the M0 picks in this location immediately to the east of the fracture zone bends. Talwani et al.'s (2016) interpretation of the Wharton Basin fracture zone bends also did not take into account the seafloor age of 101 ± 1 Ma obtained from DSDP Site 256 (Davies et al. 1974) that directly overlaps the fracture zone bends, which is in excellent agreement with the more recently acquired date for the Dirck Hartog Ridge (Whittaker et al. 2016).

In conclusion, it is impossible, in terms of tectonic evolution, for an extinct Dirck Hartog Ridge, with an age of 102.3 ± 2.5 Ma (Whittaker et al. 2016), to be located east of Wharton basin fracture zone bends, if those bends formed from a reorganization at approximately 118–117 Ma. A variety of other plate motion changes, as well as Australia-Antarctica and India-Madagascar breakup, occurred in the mid-Cretaceous and coincide with the final breakup between Africa and South America in the equatorial Atlantic (Somoza and Zaffarana 2008), lending additional support to an approximately 100 Ma age of the major fracture zone bends between India and Australia. Finally, an onset of India's northward motion at 118 Ma, instead of around 100 Ma, is also irreconcilable with models for the separation of India from Madagascar. The breakup and spreading history of India and Madagascar is intimately linked to India's change in motion (Gibbons et al. 2013). Their separation initiated around approximately 100 Ma, following the approximately 100 Ma reorganization, and culminated in seafloor spreading from south to north from 94 to 84 Ma (Gibbons et al. 2013). An interpretation of VGG seafloor images supplemented with marine geological and geophysical ship data allows us to robustly map the tectonic history of the ocean basins, even within the CNS.

16.4.3   WHAT CAUSED THE 100 MA EVENT?

Several authors have speculated about what drove a major plate reorganization at approximately 105–100 Ma. Zahirovic et al. (2016) recently proposed that commencement of Indian Plate subduction following a ridge subduction event at its northern margin may have triggered the spreading reorganization recorded in the Wharton Basin fracture zones. In this scenario, the Neotethyan spreading ridge that formed the northern margin of the Indian Plate since approximately 155 Ma was subducted at the intraoceanic Kohistan-Ladakh subduction zone from approximately 110–90 Ma, producing a significant phase of magmatic accretion from approximately 105–99 Ma, high-temperature granulite facies metamorphism at approximately 95 Ma, and a hot mantle source at the Kohistan Arc. This ridge subduction event would have changed the balance of plate-driving forces acting on the Indian Plate; in particular, it strengthened northward slab pull, to which the Australian-Indian and Antarctic-Indian spreading ridges responded by clockwise rotation, as reflected in the major fracture zone bends.

16.5   MAPPING SUB-SEAFLOOR TECTONIC FABRIC

Marine gravity anomalies derived from satellite altimetry have been used to help delineate the boundary between continental and oceanic crust (COB) (Pawlowski 2008) as well as regional fault systems on stretched continental crust (McGrane et al. 2001; Trung et al. 2004). However, the

most recent satellite-derived vertical gravity gradient grid (Sandwell et al. 2014) allows the detailed mapping of relatively closely-spaced faults (less than 10 km), in contrast to most previous applications. Here, we focus on two examples where the new generation of gravity data can be used to map regional fault systems at scales that were previously achieved only by relatively closely spaced seismic reflection profiles.

16.5.1 North Falkland Basin

Our first example is the North Falkland Basin, which is embedded in the northern portion of the Falkland Plateau (Figure 16.8). The basin is located north of the Falkland Islands (Figure 16.10). Strain rate inversion of its stratigraphy has shown that the basin formed during a single phase or rifting close to the Jurassic-Cretaceous boundary, lasting from about 150–125 Ma (Jones et al. 2004). Its structural fabric has been mapped based on seismic reflection data (Richards and Hillier 2000) (Figure 16.11), an interpretation that was recently refined by Lohr and Underhill (2015).
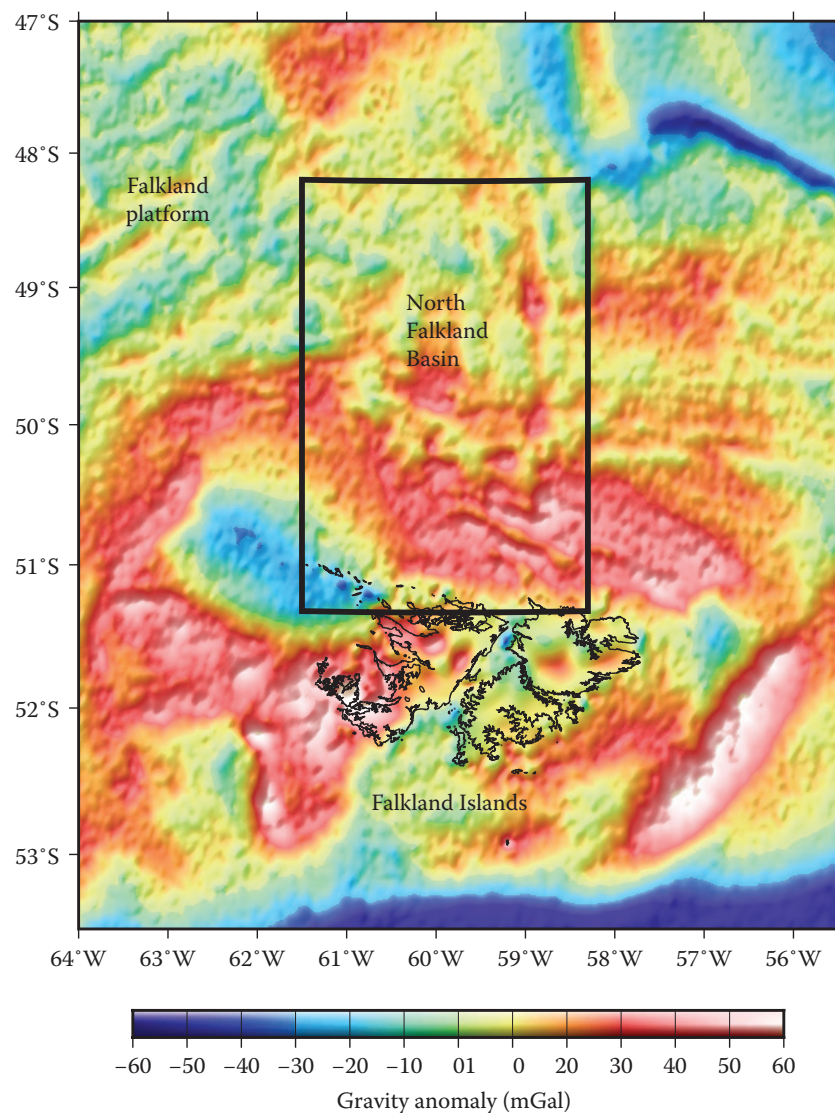
FIGURE 16.10 Free-Air Gravity Anomalies of The Falkland Plateau. Free-air gravity anomaly map of the Falkland Plateau. Black box outlines the region shown in Figure 16.11.
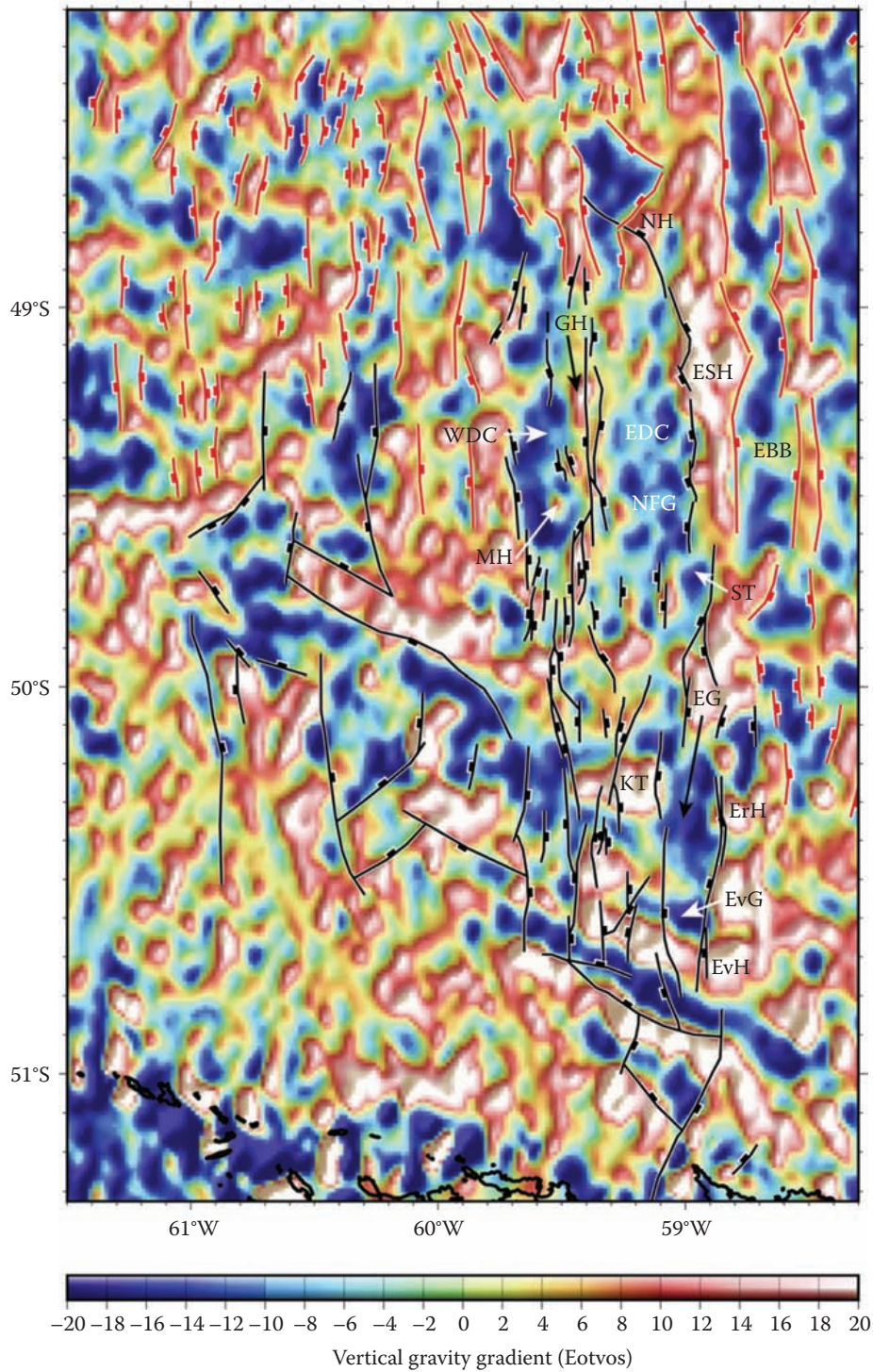
FIGURE 16.11 Vertical Gravity Gradient and Structural Fabric of The North Falkland Basin. Vertical gravity gradient (VGG) map (Sandwell et al. 2014) of the North and South Falkland Basins (see Figure 16.10 for location). Black fault interpretations are from Richards and Hillier (2000), and faults shown in red are interpreted from the VGG, with filled boxes indicating the dip direction. Note good correlation between linear, positive VGG anomalies and elevated blocks bounded by normal faults interpreted by Richards and Hillier (2000). NFB, North Falkland Basin; ESH, Eastern Structural High; EBB, Eastern Backarc-Basin; KT, Keppel Terrace; EG, Ernest Graben; ErH Ernest High; EvH, Evie High; EvG, Evie Graben; EDC, Eastern Depo-Centre; IGH, Intra-Graben High; MH, Minke High; WDC, Western Depo-Centre; ST, Sanson Terrace; NH, Northern High.

This is a good area to ground-truth the VGG data for the interpretation of buried structures as it is quite well mapped. The fault interpretation of Richards and Hillier (2000) is overlain over the VGG on Figure 16.11 and illustrates an excellent correlation between normal faults interpreted to bound structural basement highs and the edges of positive VGG anomalies, illustrating that an interpretation based just on the VGG data would provide a fairly similar result. In Figure 16.9, we have extended the interpretation of Richards and Hillier (2000) to the north, east, and west, following the assumption that VGG highs correspond to structural basement highs and are bounded by normal faults. This example demonstrates the power of the new VGG data to interpret buried basement fault fabrics in frontier areas with poor seismic data coverage.

16.5.2 LORD HOWE RISE

Our next example represents a deep water frontier area, namely the Lord Howe Rise, a stretched, submerged continental plateau with poor seismic data coverage (Bache et al. 2014). The most comprehensive regional structural interpretation can be found in Collot et al. (2009) and is shown in Figure 16.10. It outlines major troughs and highs in the region, as well as some regional transcurrent faults offsetting the main structural fabric oriented north-south to northwest-southeast (Figure 16.12). The Lord Howe Rise falls into the category of wide, asymmetric rifts, with a width of about 200 km, while the conjugate Australian margin is extremely narrow. Brune et al. (2014) recently suggested that such hyperextended crust typical for wide, asymmetric rifts is produced by steady-state rift migration. Rift migration in a succession of phases is accomplished by sequential, oceanward-younging, upper crustal faults, and is balanced through lower crustal flow. This process results in a dense network of faults dissecting a "basin and range" basement fabric as is clearly seen in the VGG image for the Lord Howe Rise (Figure 16.12), where VGG highs outline horst blocks while VGG lows delineate basement troughs. We have used the VGG image, following the insights gained from the North Falkland Basin interpretation, to interpret the distributed fault fabric of this wide rift. This is the first regional structural map of this region, which may form a useful framework for future seismic imaging as well as scientific drilling by the Integrated Ocean Drilling Program planned for 2017.

16.6 CONCLUSIONS AND FUTURE OUTLOOK

The current generation of altimetry data have yielded a new marine gravity anomaly grid with an improvement in signal-to-noise ratio by a factor of two; this advance has been critical in imaging small-scale seafloor and sub-seafloor features that were previously too noisy to interpret. The new data have enabled the identification of extinct spreading ridges buried deeply beneath thick sediments (Sandwell et al. 2014) as well as previously unknown paleo-microplates in the Indian (Matthews et al. 2016) and Pacific oceans. Deeply buried basement fault fabrics along continental margins and submerged continental plateaus can now be clearly mapped in vertical gravity gradient images, representing a major advance for mapping deep-water frontier regions where seismic data are sparse and expensive to obtain. The future merging of the latest marine satellite-derived gravity grid with the Gravity Field and Steady-State Ocean Circulation Explorer (GOCE) gravity field on continents should result in improved continental fit reconstructions (e.g., Braitenberg 2015).
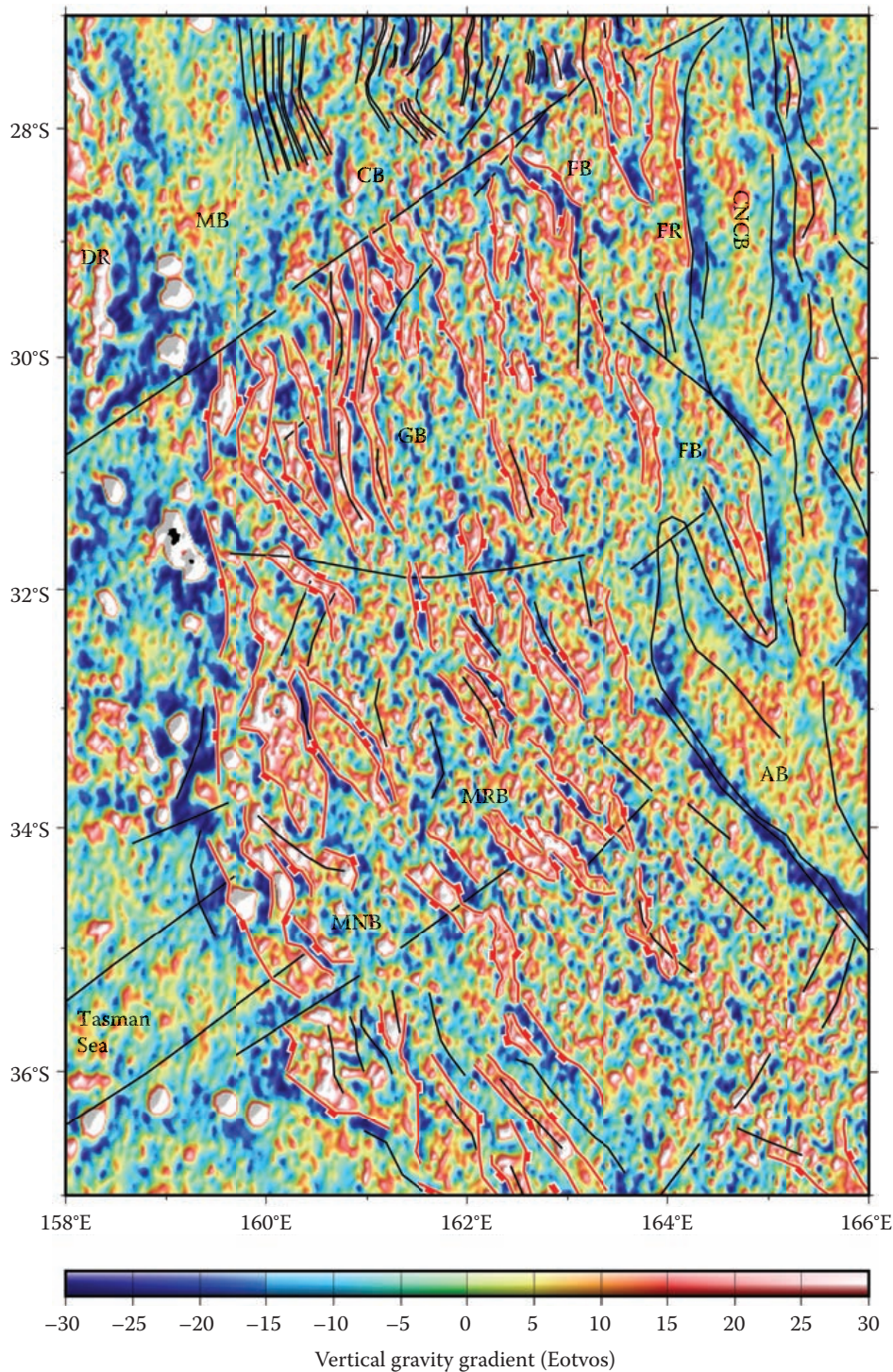
FIGURE 16.12 Vertical Gravity Gradient and Structural Fabric Of The Lord Howe Rise. Vertical gravity gradient (VGG) map (Sandwell et al. 2014) of the Lord Howe Rise, a stretched, submerged continental plateau east of Australia. The Lord Howe Rise stretches from the eastern edge of the Tasman Sea in the west to the edge of the Fairway Basin (FB) and Aotea Basin (AE) to the east. Tectonic lineaments shown as black lines are taken from Collot et al. (2009), while red lines correspond to normal faults interpreted from the VGG image, with filled boxes indicating the dip direction. DR, Dampier Ridge; MB, Middleton Basin; CP , Capel Basin; FB, Faust Basin; GB, Gower Basin; MRB, Moore Basin; MNB, Monowai Basin; FR, Fairway Ridge; CNCB, Central New Caledonia Basin.

REFERENCES

Andersen, O.B., and P. Knudsen. 1998. Global marine gravity field from the ERS-1 and GEOSAT geodetic mission altimetry. *Journal of Geophysical Research: Oceans* 103 (C4): 8129–8137.

Bache, F., N. Mortimer, and R. Sutherland, et al. 2014. Seismic stratigraphic record of transition from Mesozoic subduction to continental breakup in the Zealandia sector of eastern Gondwana. *Gondwana Research* 26 (3): 1060–1078.

Bernard, A., M. Munschy, Y. Rotstein, and D. Sauter. 2005. Refined spreading history at the Southwest Indian Ridge for the last 96 Ma, with the aid of satellite gravity data. *Geophysical Journal International* 162: 765–778.

Bird, R.T., and D.F. Naar. 1994. Intratransform origins of mid-ocean ridge microplates. *Geology* 22 (11): 987–990.

Bird, R.T., S.F. Tebbens, M.C. Kleinrock, and D.F. Naar. 1999. Episodic triple-junction migration by rift propagation and microplates. *Geology* 27 (10): 911–914.

Braitenberg, C. 2015. Exploration of tectonic structures with GOCE in Africa and across-continents. *International Journal of Applied Earth Observation and Geoinformation* 35: 88–95.

Brune, S., C. Heine, M. Pérez-Gussinyé, and S.V. Sobolev. 2014. Rift migration explains continental margin asymmetry and crustal hyper-extension. *Nature Communications* 5: 1–9.

Cazenave, A., P. Schaeffer, M. Berge, C. Brossier, K. Dominh, and M.C. Gennero. 1996. High-resolution mean sea surface computed with altimeter data of ERS-1 (Geodetic Mission) and TOPEX-POSEIDON. *Geophysical Journal International* 125 (3): 696–704.

Chelton, D.B., J.C. Ries, B.J. Haines, L.-L. Fu, and P.S. Callahan. 2001. Satellite altimetry. *International Geophysics* 69: 1–ii.

Collot, J., R. Herzer, Y. Lafoy, and L. Geli. 2009. Mesozoic history of the Fairway-Aotea Basin: Implications for the early stages of Gondwana fragmentation. *Geochemistry, Geophysics, Geosystems* 10 (12).

Davies, T.A., B.P. Luyendyk, K.S. Rodolfo, et al., eds. 1974. *Leg XXVI, Initial reports of the Deep Sea Drilling Project.* Vol. 26. Washington, DC: US Govn't Printing Office.

Desa, M.A., and M.V. Ramana. 2016. Middle cretaceous geomagnetic field anomalies in the eastern Indian Ocean and their implication to the tectonic evolution of the Bay of Bengal. *Marine Geology* 382: 111–121.

Eagles, G., and M. König. 2008. A model of plate kinematics in Gondwana breakup. *Geophysical Journal International* 173 (2): 703–717.

Eakins, B.W. 2002. *Structure and Development of Oceanic Rifted Margins, Earth Sciences.* University of California, San Diego, CA.

Gaina, C., R.D. Müller, B. Brown, T. Ishihara, and S. Ivanov. 2007. Breakup and early seafloor spreading between India and Antarctica. *Journal of Geophysics International* 170 (1): 151–170.

Garcia, E.S., D.T. Sandwell, and W.H.F. Smith. 2014. Retracking CryoSat-2, Envisat and Jason-1 radar altimetry waveforms for improved gravity field recovery. *Geophysical Journal International* 196 (3): 1402–1422. doi: 10.1093/gji/ggt469.

Gee, J.S., and D.V. Kent. 2007. Source of Oceanic magnetic anomalies and the geomagnetic polarity times-cale. *Treatrise Geophys* 5: 455–507.

Gibbons, A.D., J.M. Whittaker, and R.D. Müller. 2013. The breakup of East Gondwana: Assimilating con-straints from Cretaceous ocean basins around India into a best-fit tectonic model. *Journal of Geophysical Research: Solid Earth* 118 (3): 808–822.

Goff, J.A., and J.R. Cochran. 1996. The Bauer scarp ridge jump: A complex tectonic sequence revealed in satellite altimetry. *Earth and Planetary Science Letters* 141 (1): 21–33.

Granot, R., J. Dyment, and Y. Gallet. 2012. Geomagnetic field variability during the Cretaceous Normal Superchron. *Nature Geoscience* 5 (3): 220–223.

Haxby, W.F., G.D. Karner, J.L. LaBrecque, and J.K. Weissel. 1983. Digital images of combined oceanic and continental data sets and their use in tectonic studies. *Eos, Transactions American Geophysical Union* 64 (52): 995–1004.

Hey, R.N. 1977. A new class of "pseudo faults" and their bearing on plate tectonics: A propagating rift model. *Earth and Planetary Science Letters* 37 (2): 321–325.

Hey, R.N. 2004. Propagating rifts and microplates at mid-ocean ridges. In *Encyclopedia of Geology*, edited by R.C. Selley, R. Cocks, and I. Plimer. London: Academic Press, pp. 396–405.

Hey, R.N., F.K. Duennebier, and W.J. Morgan. 1980. Propagating rifts on midocean ridges. *Journal of Geophysical Research* 85 (B7): 3647–3658.

Hey, R.N., H.W. Menard, T.M. Atwater, and D.W. Caress. 1988. Changes in direction of seafloor spreading revisited. *Journal of Geophysical Research* 93 (B4): 2803–2811.

Hey, R.N., D.F. Naar, M.C. Kleinrock, W.J. Phipps Morgan, E. Morales, and J.-G. Schilling. 1985. Microplate tectonics along a superfast seafloor spreading system near Easter Island. *Nature* 317: 320–325.

Hwang, C., and B. Parsons. 1996. An optimal procedure for deriving marine gravity from multi-satellite altimetry. *Geophysical Journal International* 125 (3): 705–718.

Jones, S.M., N. White, P. Faulkner, and P. Bellingham. 2004. Animated models of extensional basins and passive margins. *Geochemistry, Geophysics, Geosystems* 5 (8).

Lohr, T., and J.R. Underhill. 2015. Role of rift transection and punctuated subsidence in the development of the North Falkland Basin. *Petroleum Geoscience* 21 (2–3): 85–110.

Mammerickx, J., D.F. Naar, and R.L. Tyce. 1988. The mathematician paleoplate. *Journal of Geophysical Research* 93 (B4): 3025–3040.

Marks, K.M., and A.A. Tikku. 2001. Cretaceous reconstructions of East Antarctica, Africa and Madagascar. *Earth & Planetary Science Letters* 186 (3–4): 479–495.

Matthews, K.J., R.D. Müller, and D.T. Sandwell. 2016. Oceanic microplate formation records the onset of India–Eurasia collision. *Earth and Planetary Science Letters* 433: 204–214.

Matthews, K.J., R.D. Müller, P. Wessel, and J.M. Whittaker. 2011. The tectonic fabric of the ocean basins. *Journal of Geophysical Research* 116 (B12): B12109.

Matthews, K.J., M. Seton, and R.D. Müller. 2012. A global-scale plate reorganization event at 105–100 Ma. *Earth & Planetary Science Letters* 355: 283–298.

Maus, S., C.M. Green, and J.D. Fairhead. 1998. Improved ocean-geoid resolution from retracked ERS-1 satellite altimeter waveforms. *Geophysical Journal International* 134 (1): 243–253.

McGrane, K., P.W. Readman, and B.M. O'Reilly. 2001. Interpretation of transverse gravity lineaments in the Rockall Basin. *Geological Society, London, Special Publications* 188 (1): 393–399.

Müller, R.D., D. Mihut, and S. Baldwin. 1998. A new kinematic model for the formation and evolution of the Northwest and West Australian margin. In *The Sedimentary Basins of Western Australia 2*, edited by P.G. Purcell and R.R. Purcell. Perth: Petroleum Exploration Society of Australia.

Müller, R.D., W.R. Roest, J.-Y. Royer, L.M. Gahagan, and J.G. Sclater. 1997. Digital isochrons of the world's ocean floor. *Journal of Geophysical Research: Solid Earth* 102 (B2): 3211–3214.

Müller, R.D., M. Seton, S. Zahirovic, et al. 2016. Ocean basin evolution and global-scale plate reorganization events since Pangea breakup. *Annual Review of Earth and Planetary Sciences* 44: 107–138.

Olgiati, A., G. Balmino, M. Sarrailh, and C.M Green. 1995. Gravity anomalies from satellite altimetry: Comparison between computation via geoid heights and via deflections of the vertical. *Bulletin Géodésique* 69 (4): 252–260.

Pawlowski, R. 2008. The use of gravity anomaly data for offshore continental margin demarcation. *The Leading Edge* 27 (6): 722–727.

Phipps Morgan, J., and E.M. Parmentier. 1985. Causes and rate-limiting mechanisms of ridge propagation: A fracture mechanics model. *Journal of Geophysical Research* 90 (B10): 8603–8612.

Powell, C., S.R. Roots, and J.J. Veevers. 1988. Pre-breakup continental extension in East Gondwanaland and the early opening of the eastern Indian Ocean. *Tectonophysics* 155: 261–283.

Richards, P.C., and B.V. Hillier. 2000. Post-drilling analysis of the North Falkland Basin – Part 1: Tectono-stratigraphic framework. *Journal of Petroleum Geology* 23 (3): 253–272.

Rotstein, Y., M. Munschy, and A. Bernard. 2001. The Kerguelen Province revisited: Additional constraints on the early development of the Southeast Indian Ocean. *Marine Geophysical Researches* 22 (2): 81–100.

Rusby, R.I., and R.C. Searle. 1993. Intraplate thrusting near the Easter microplate. *Geology* 21 (4): 311–314.

Sandwell, D.T., R.D. Müller, W.H.F. Smith, E. Garcia, and R. Francis. 2014. New global marine gravity model from CryoSat-2 and Jason-1 reveals buried tectonic structure. *Science* 346 (6205): 65–67.

Sandwell, D.T., and W.H.F. Smith. 1997. Marine gravity anomaly from GEOSAT and ERS 1 satellite altimetry. *Journal of Geophysical Research: Solid Earth* 102 (B5): 10039–10054.

Sandwell, D.T., and W.H.F. Smith. 2005. Retracking ERS-1 altimeter waveforms for optimal gravity field recovery. *Geophysical Journal International* 163 (1): 79–89.

Sandwell, D.T., and W.H.F. Smith. 2009. Global marine gravity from retracked GEOSAT and ERS-1 altimetry: Ridge segmentation versus spreading rate. *J. Geophys. Res.* 114 (B1): B01411.

Sandwell, D.T., W.H.F. Smith, S. Gille, et al. 2006. Bathymetry from space: Rationale and requirements for a new, high-resolution altimetric mission. *Comptes Rendus Geoscience* 338 (14): 1049–1062.

Schouten, H., K.D. Klitgord, and D.G. Gallo. 1993. Edge-driven microplate kinematics. *Journal of Geophysical Research: Solid Earth* 98 (B4): 6689–6701.

Searle, R. 2013. *Mid-ocean ridges*. Cambridge University Press.

Ségoufin, J., P. Munschy, P. Bouysse, et al. 2004. *Map of the Indian Ocean (1:20 000 000), sheet 1: "Physiography," sheet 2: "Structural map."* Commission for the Geological Map of the World, Paris.

Smith, W.H.F. 2015. Resolution of seamount geoid anomalies achieved by the SARAL/AltiKa and Envisat RA2 satellite radar altimeters. *Marine Geodesy* 38 (Suppl. 1): 644–671.

Somoza, R., and C.B. Zaffarana. 2008. Mid-cretaceous polar standstill of South America, motion of the Atlantic hotspots and the birth of the Andean cordillera. *Earth and Planetary Science Letters* 271 (1): 267–277.

Talwani, M., M.A. Desa, M. Ismaiel, and K.S. Krishna. 2016. The Tectonic origin of the Bay of Bengal and Bangladesh. *Journal of Geophysical Research: Solid Earth* 121 (7): 4836–4851.

Tapley, B.D., and M.-C. Kim. 2001. Applications to geodesy. In *Satellite Altimetry and Earth Sciences*, edited by L.-L. Fu and A. Cazenave. New York: Academic Press.

Tebbens, S.F., and S.C. Cande. 1997. Southeast Pacific tectonic evolution from early oligocene to present. *Journal of Geophysical Research* 102 (B6): 12061–12084.

Trung, N.N., S.-M. Lee, and B.C. Que. 2004. Satellite gravity anomalies and their correlation with the major tectonic features in the South China Sea. *Gondwana Research* 7(2): 407–424.

Veevers, J.J. 2000. Change of tectono-stratigraphic regime in the Australian plate during the 99 Ma (mid-Cretaceous) and 43 Ma (mid-Eocene) swerves of the Pacific. *Geology* 28 (1): 47–50.

Watson, S.J., J.M. Whittaker, J.A. Halpin, et al. 2016. Tectonic drivers and the influence of the Kerguelen plume on seafloor spreading during formation of the early Indian Ocean. *Gondwana Research* 35: 97–114.

Wessel, P. 2001. Global distribution of seamounts inferred from gridded GEOSAT/ERS-1 altimetry. *Journal of Geophysical Research: Solid Earth* 106 (B9): 19431–19441.

Wessel, P., K.J. Matthews, R.D. Müller, et al. 2015. Semiautomatic fracture zone tracking. *Geochemistry, Geophysics, Geosystems* 16 (7): 2462–2472.

Whittaker, J.M., J.C. Afonso, S. Masterton, et al. 2015. Long-term interaction between mid-ocean ridges and mantle plumes. *Nature Geoscience* 8 (6): 479–483.

Whittaker, J.M., S.E Williams, J.A. Halpin, et al. 2016. Eastern Indian Ocean microcontinent formation driven by plate motion changes. *Earth and Planetary Science Letters* 454: 203–212.

Williams, S.E., J.M. Whittaker, R. Granot, and D.R. Müller. 2013. Early India-Australia spreading history revealed by newly detected Mesozoic magnetic anomalies in the Perth Abyssal Plain. *Journal of Geophysical Research: Solid Earth* 118 (7): 3275–3284.

Wingham, D.J., C.R. Francis, S. Baker, et al. 2006. CryoSat: A mission to determine the fluctuations in Earth's land and marine ice fields. *Advances in Space Research* 37 (4): 841–871.

Wright, N.M., M. Seton, S.E. Williams, and R.D. Müller. 2016. The late cretaceous to recent tectonic history of the Pacific Ocean basin. *Earth-Science Reviews* 154: 138–173.

Zahirovic, S., K.J. Matthews, N. Flament, et al. 2016. Tectonic evolution and deep mantle structure of the eastern Tethys since the latest Jurassic. *Earth Science Reviews* 162: 293–337.

Zhang, S., and D.T. Sandwell. 2016. Retracking of SARAL/AltiKa radar altimetry waveforms for optimal gravity field recovery. *Marine Geodesy*.